

Boosting visible-light-driven photocatalytic performance of waxberry-like CeO₂ by samarium doping and silver QDs anchoring

| | |
|------------------------------|--|
| 著者 | Yang Hui, Xu Bin, Zhang Qitao, Yuan Saisai, Zhang Zhipeng, Liu Yiting, Nan Zhaodong, Zhang Ming, Ohno Teruhisa |
| journal or publication title | Applied Catalysis B: Environmental |
| volume | 286 |
| page range | 119845-1-119845-9 |
| year | 2021-01-01 |
| その他のタイトル | Boosting visible-light-driven photocatalytic performance of waxberry-like CeO ₂ by samarium doping and silver QDs anchoring |
| URL | http://hdl.handle.net/10228/00009045 |

doi: <https://doi.org/10.1016/j.apcatb.2020.119845>

Boosting visible-light-driven photocatalytic performance of waxberry-like CeO₂ by samarium doping and silver QDs anchoring

Hui Yang^{a, d}, Bin Xu^{*, a}, Qitao Zhang^{*, b}, Saisai Yuan^c, Zhipeng Zhang^a, Yiting Liu^b, Zhaodong Nan^a, Ming Zhang^a, Teruhisa Ohno^{*, d}

^a School of Chemistry and Chemical Engineering, Yangzhou University, Yangzhou 225002, China

^b International Collaborative Laboratory of 2D Materials for Optoelectronics Science and Technology of Ministry of Education, Institute of Microscale Optoelectronics, Shenzhen University, Shenzhen, 518060, China

^c Collaborative Innovation Center of Chemistry for Energy Materials, Department of Chemical and Biochemical for Energy Materials, Department of Chemical and Biochemical Engineering, College of Chemistry and Chemical Engineering, Xiamen University, Xiamen 361005, China

^d Department of Applied Chemistry, Faculty of Engineering, Kyushu Institute of Technology, Kitakyushu 804-8550, Japan

Corresponding Author: *Bin Xu (tw@yzu.edu.cn), *Qitao Zhang (qitao-zhang@szu.edu.cn), or *Teruhisa Ohno (tohno@che.kyutech.ac.jp).

Author Contributions: ‡ Hui Yang and Bin Xu. These authors contributed equally.

Abstract: In this work, waxberry-like CeO₂ photocatalyst (denoted ASC) with prominent visible-light-driven photocatalytic performances for multi-model reactions was achieved by Sm doping and Ag quantum dots (QDs) anchoring. For instance, the as-fabricated ASC acquired 7.08-times and 6.83-times higher activities for CH₃CHO removal and H₂ production than those of pure CeO₂ counterpart, respectively. The concentration of oxygen vacancies (O_v) in CeO₂ is distinctly increased by Sm doping, resulting in a narrower bandgap of the Sm-doped CeO₂ (SC). Under visible light irradiation, the O_v caused by doping can capture the photo-excited electrons and construct a doping-related transition state between the conduction band (CB) and the valence band (VB), which can effectively limit the recombination of photo-excited electrons and holes. These captured electrons further fleetly transfer to the co-catalytic sites of anchored Ag QDs, strengthening the absorption utilization for visible-light synchronously. The migration of charge carriers and proposed mechanisms were well elaborated by transient photovoltage (TPV), surface photovoltage (SPV) and density functional theory (DFT) calculation. It is hoped our work in this paper could provide potential and meaningful strategies for the design of noble metal quantum dots modified metal oxide semiconductors and facilitate their applications in other photocatalytic fields effectively.

Keywords: Doped-CeO₂, Transition state, Silver quantum dots, Heterogeneous interface, Photocatalysis

1. Introduction

Solar-driven reactions are unique examples of sustainable chemistry and one of the prerequisites of these reactions is to develop cost-effective materials with excellent solar-trapping and solar energy conversion efficiency [1-3]. Hence, visible-light responsive efficient photocatalysts are desirable demand for effective photocatalytic process. In the past few decades, photocatalytic applications of CeO₂ have attracted increasing interest due to its unique structural properties such as unique fluorite-type structure, rigid skeleton and distinct capacity of oxygen storage by flexible conversion among cerium's tetravalent and trivalent valence states [4-7]. Earlier, our group has successfully synthesized CeO₂ with different morphologies to enhance its photocatalytic performance, and CeO₂ with spherical morphology was found to be most favorable for the photocatalytic reactions due to its larger surface area and strong adsorption capacity [8-10]. However, own to its wide bandgap, visible-light absorption of CeO₂ is extremely weak, which obviously limits its potential applications [11, 12]. Various methods have been applied to enhance the absorption ability of visible light in ceria and among them effective formation of heterogeneous photocatalysts has distinct advantages like wide spectral response range, stability and reusability [13, 14]. It has been found that the introduction of noble metals like Au, Pt, and Pd in the matrix of CeO₂ semiconductor can achieve better response towards sunlight as a result of interfacial interaction between the active metal species and CeO₂ [14, 15]. For instance, Carltonbird et al. and Ye et al. have reported synthetic routes for the preparation of gold/ceria with different and coordinated morphologies as well as rod-shaped Au/CeO₂ product having improved photocatalytic performance under visible light [16, 17]. Thus, it is worth investigating the noble metal-metal oxide interactions in the hetero-structured photocatalysts [13-18, 19].

There have been literature reports on the application of different noble metal modified CeO₂

as photocatalysts. But prohibitive cost of most of the noble-metal based catalysts prevents their real applications. As is known, silver (Ag) is non-toxic, relatively cheap and stable in comparison to the other noble metals, resulting in wide applications in various fields [20, 21]. And it is also remarkable to find that Ag exhibits obvious localized surface plasmon resonance (LSPR) phenomenon under visible light illumination [22]. During the preparation of metal oxide supported catalysts via impregnation and high-temperature sintering processes for activation is required in order to reinforce the interfacial interactions among the noble metals and the metal oxide. In this high-temperature annealing process, a reunion of the noble metals particles and the oxide support is inevitable, which brings about a decrease in catalytic activity in a significant way [23]. Additionally, some of the reported hydrothermal methods are constituted of complicated steps or the addition of harmful materials. The problems can be avoided using quantum dots of the noble metals having a very tiny size and uniform distribution to anchor to the support under mild reaction conditions. This might result in higher catalytic performance as a result of strengthened interfacial interactions. Besides, doping of rare earth (RE) metal ions can also effectively improve the performance of pure CeO₂ [24, 25]. Among various RE metals, samarium (Sm) is more suitable because its crystalline quality of bulk ionic conductors is much closer to cerium, which is significant for ionic conductivity enhancement in doping heterostructures [26]. It is aimed to form CeO₂-based products with a crystal-expanded structure, which is more convenient for electronic transmission [27].

Herein, Sm-doped CeO₂ material anchored with Ag QDs (ASC) was prepared by template-free hydrothermal method. The as-prepared ASC photocatalyst with a waxberry-like morphology affords abundant active sites for multi-purpose photocatalytic applications, such as water-splitting, gaseous and aqueous (acetaldehyde, bisphenol A and 4-nitrophenol) refractory pollutant removal.

The heterogeneous photocatalytic performances can be remarkably facilitated by conveniently adjusting the interfacial interactions between Ag and Sm-CeO₂. The morphology, crystal and optical properties as well as the separation mechanism of charge carriers were characterized by various advanced spectroscopic technologies. This work makes us adopt an effective strategy to elevate the photocatalytic performance of the other Ce-based heterogeneous photocatalyst.

2. Experimental Details

General procedures for the synthesis of Ag@Sm-CeO₂

First, 4.0 mmol of cerium nitrate hexahydrate (Ce(NO₃)₃·6H₂O, 1.737 g), 0.4 mmol samarium nitrate hexahydrate (Sm(NO₃)₃·6H₂O, 0.178 g) and 0.8 mmol polyvinyl pyrrolidone (PVP) were dissolved in an aqueous of ethanol (40 mL), glycol (80 mL) and deionized H₂O (20 mL). Then the mixture was stirring at room temperature for one hour. Then, 3 wt% silver nitrate (AgNO₃, 0.052 g) was added into the aqueous and stirred for another two hours. Then, the above mixture was infunded into a 200 mL reaction kettle lined with Teflon and kept the heat of 180 °C for 20 h. After the temperature naturally dropping down, the fresh sediment was obtained by centrifugal separation, washed with mixed aqueous of deionized water and ethanol (1:1, volume ratio) for three times, respectively. Later, it was dried in the oven under 70 °C for 12 h to collect the yellow precursor. Finally, the as-prepared precursors were calcinated in a muffle furnace under 500 °C for four hours to obtain the final product, which was denoted as silver quantum dots modified samarium-doped CeO₂ (Ag@Sm-CeO₂, ASC).

For comparison experiments, the as-fabricated pure CeO₂, samarium-doped CeO₂ and silver quantum dots modified CeO₂ materials were also obtained under the same conditions and the products were denoted as CeO₂, SC and AC simply.

3. Results and Discussion

3.1 Morphology characterization

Here is Figure 1.

The morphology information of the synthesized products was expressed by HRTEM together with SEM. Pure CeO₂ shows smooth microspheres morphology with a diameter of ca. 200nm (Figure 1a). The SC still maintains a spherical morphology with a similar diameter (Figure 1b). However, a distinct change of the rough waxberry-like morphology can be clearly observed in AC and ASC (Figure 1c and d). This phenomenon can be assigned to the attachment of the Ag QDs (ca. 2 nm) with a good distribution on the surface of the SC microspheres (Figure 1e). The related changes in the morphology also can be seen in the SEM images of Figure S1. Noticeable lattice fringes containing an inter-planar distance of 0.325 nm and 0.240 nm are seen in ASC, which are belonged to the (111) crystal plane of the face-centered cubic CeO₂ and (111) crystal plane of the cubic Ag, respectively (Figure 1f). The EDS-mapping images clearly show the presence of the elements Ag, Ce, O and Sm on the waxberry-like ASC microspheres and they are well distributed (Figure S2). Considering the above analysis, it can deduce that the photocatalyst of ASC was primarily synthesized by a template-less solvothermal method.

3.2 Structural characterization

Here is Figure 2.

The crystal phase and structural information of the as-formed samples were determined from the XRD patterns. The presence of the cubic phase of Ag (JCPDS. No. 65-2871) and the face-centered cubic phase of CeO₂ (JCPDS. No. 43-1002) can be simultaneously observed in both ASC and AC (Figure 2a) [21, 28]. The characteristic diffraction peaks are located at 37.99°, 44.18° and

64.35°, which are assigned to the (111), (200) and (220) crystal faces of Ag, respectively. At the same time, the characteristic peaks of ceria corresponding to the crystal faces of (111), (200), (220) and (311) are situated at a degree of 28.54°, 33.07°, 47.48° and 56.36°, respectively [29]. Generally, the acuminate diffraction peaks of all the products indicate a high crystallinity and purity. The similarity of the peaks observed for AC and ASC proves the addition of these samarium ions possesses a negligible influence on the crystalline quality of those doped photocatalysts. Nevertheless, compared with pure CeO₂, the peak corresponding to (111) plane in the ASC shifts from 28.45° to a lower angle of 28.40° after Sm ions doping (detailed inset in [Figure 2b](#)). This phenomenon indicates that the doping of Sm in the crystal lattice of SC leads to lattice expansion [28]. On the contrary, after Ag addition, the peak for the (111) peak shifts to a higher angle of 28.70° in the sample ASC. It indicates that further growth of CeO₂ crystal seed is restricted by the Ag nanoparticles loaded on the surface of CeO₂, resulting in steric hindrance effects to a contraction of the crystal lattice in AC. Hence, the middle position of the (111) peak of ASC (28.58°) located between AC (28.70°) and CeO₂ (28.45°) can be reasonably understood.

Further, for the sake of determining the actual doping information of these Sm ions, Rietveld refinements calculation was also carried out ([Figure S3](#)) [8, 9, 29]. Compared with pure CeO₂ (5.4100 Å), the numerical value of the lattice parameter (a) of SC is changed to 5.4217Å ([Table S1](#)). A higher value of (a) means that the lattice of CeO₂ was successfully accessed by Sm and thereby resulting in the expansion of the crystal lattice of CeO₂ [8, 28]. Further, the lattice parameter of ASC (5.4209 Å) is smaller than SC, which owns an excellent match with results of above XRD patterns.

Structural defects are effectively characterized by Raman spectra. An apparent peak at 462 cm⁻¹ is assigned to a forceful F_{2g} symmetry mode as illustrated in fluorite phase CeO₂ ([Figure 2](#)).

After different contents of Sm doping (Figure S4a), the other two weak peaks of 540 cm^{-1} and 600 cm^{-1} further observed and these two peaks are attributed to the doping-related extrinsic oxygen vacancies (R_{dopant}) and partial Ce-O ($R_{\text{Ce-O}}$) bond symmetry stretch, respectively [9, 29]. Moreover, the position of the F_{2g} peak remains the same Raman shift after different contents of Ag anchoring signifying that the MO_8 structure of CeO_2 is well maintained (Figure S4b). Part of cerium atoms is substituted by the samarium, resulting in external oxygen vacancies. The relative concentration ratios of (O_v) are calculated from Eq. (1):

$$O_v\% = \frac{\text{Area}[R_{\text{Ce-O}}+R_{\text{dopant}}]}{\text{Area}(F_{2g})} * 100\%, \quad (1)$$

The related calculation results are shown in Table S2. The value of (O_v) reaches 16.89% in ASC, which is much higher than the other samples, and this result is also consistent with the XPS O1s analysis as discussed below.

Here is Figure 3.

The surface composition, chemical state of the elements and the interaction among the elements were detected by XPS analysis. As evident from a survey spectra of the ASC photocatalyst (Figure S5), the presence of Ce, O, Ag and Sm are confirmed and it is in good consistent with the results from EDX mapping. The corresponding Ce 3d spectra can be deconvoluted and fitted into ten peaks according to Gaussian-Lorentzian function (Figure 3a). Based on the previous study, the labels of (U, V), (U_2 , V_2) as well as (U_3 , V_3) are ascribed to the characteristic peaks of Ce^{4+} in CeO_2 . Two groups bimodal involving (U_0 , V_0) and (U_1 , V_1) can be classified as characteristic peaks of Ce^{3+} , respectively. The quantified calculations of Ce^{3+} are following Eq. (2) [9, 30]:

$$[\text{Ce}^{3+}] \% = \frac{\text{Area}[\text{V}_0+\text{V}_1+\text{U}_0+\text{U}_1]}{\text{Total Area}} * 100\%, \quad (2)$$

The corresponding values obtained from the equation were also presented in [Table S2](#). Additionally, in ASC the binding energy (BE) of Ce 3d shifts to a lower value ([Figure 3b](#)), compared to other samples, indicating the formation of a heterojunction which affects the electrons density of cerium. Furthermore, in [Figure 3d](#), the peaks at 528.48 and 531.35 eV assigned to the BE of the lattice oxygen (O_L) and active surface oxygen (O_S) can be obviously detected, respectively [8, 29]. In comparison to other samples, the BE of ASC assigned to O_L and O_S also shifts to a significantly lower value ([Figure 3e](#)). After deconvolution and multimodal separation, each kind of oxygen ratio has been tabulated in [Table S2](#). Interestingly, concentrations of Ce^{3+} and O_S in ASC are found to be 25.22% and 30.81% respectively, which significantly higher than those in other samples. As well known that the existence of trivalent cerium ions suggests a defective structure of CeO_2 and creates more oxygen vacancies (O_v), which allows compensation for the doping-related charges by active surface oxygen. In a mean time, the compensated migration can accelerate the spread rate of oxygen and facilitate reactive oxygen species (ROS) to favor the formation of highly reactive radicals, which can effectively oxidize organic substances. Therefore, it can be speculated that ASC should exhibit higher photocatalytic activity.

The typical high-resolution XPS spectrum of Ag 3d is displayed in [Figure 3c](#) and the two peaks located at 368.68 eV and 373.73 eV in ASC correspond to the BE of silver's $3d_{5/2}$ and Ag $3d_{3/2}$, severally, which are assigned to metallic silver [21, 22]. Compared to the value of Ag metal (about 368.20 eV), a small shift in the BE can be ascribed to the anchoring of the Ag particles to the CeO_2 . A new energy level is formed in ASC, indicating that a heterogeneous interface developed between the Ag QDs and SC. It can evidently prove the successful synthesis of the ASC

photocatalyst. After deconvoluting and separating, the two peaks situated at BE of 1081.60 eV and 1109.23 eV can be assigned to the BE of Sm 3d5 and Sm 3d3, respectively (Figure 3f) [28]. In comparison to the SC, higher BE of Sm in ASC further indicates a strong interaction between SC and the Ag QDs.

Here is Figure 4.

UV-Vis diffuse reflectance (DRS) spectra can be applied for confirming the optic features of these products. As given in Figure 4a, the observance of the absorption peak at 438 nm in ASC and AC, which is absent in pure CeO₂ and SC, indicates that the addition of Ag can broaden the spectral response range and enhance the response capacity of the absorbed light. Besides, the absorption margin of the band for semiconductor photocatalysts follows Eq. (3) [28, 31]:

$$(\alpha h\nu)^n = B (h\nu - E_g), \quad (3)$$

Accordingly, the values of the bandgap for CeO₂, SC, AC and ASC were estimated to be 2.96, 2.91, 2.86 and 2.82 eV, respectively (Figure S6a), indicating that the doping of Sm can narrow the bandgap of CeO₂. Narrow bandgap energy is one of the pivotal parameters in evaluating the photocatalytic activity [9, 32]. The doping of Sm ions can facilitate the construction of trivalent cerium ions and generate more oxygen vacancies (O_v), and the increased proportion of O_v results in the formation of a transition state which is closer to the CB, thereby reducing the bandgap of related products. The potential of the VB was further obtained from their VB-XPS spectra (Figure S6b). These results reveal that the doping and noble metal deposition indeed have an influence on the optical properties of the samples.

The interfacial charge separation dynamics of all samples were evaluated by measuring the photo-electrochemical response. The photocurrent curves of every product sharply decreased and

increased after the illuminated light was switched off and on, respectively, suggesting an intrinsic peculiarity of semiconductor-typed photocatalysts (Figure 4b) [8, 33]. Typically, more vigorous photocurrent intensity means higher separating efficiency of the photoexcited electrons and holes. The photocurrent density of ASC reaches $402.95 \mu\text{A}/\text{cm}^2$ and shows about 11.23-, 4.66- and 1.93-times superior than that of CeO_2 , SC and AC. Notably, the related quantitative values are only 35.97 , 86.52 and $208.34 \mu\text{A}/\text{cm}^2$, respectively. And The photogenerated carriers are separated much more efficiently in ASC than other counterparts and which will result in more numbers of the separated photoinduced charges during the photocatalytic process, leading to enhanced photocatalytic performance.

Photoluminescence (PL) spectrum analysis was performed to research the recombination velocity of the electrons (e^-) and holes (h^+). Product of CeO_2 shows a stronger representative photoluminescence emission peak located at 405.75 nm and a weaker peak at 452.87 nm (Figure 4c). They may attribute to the surface defects, which are popularly situated between the VB of O_{2p} and the CB of Ce_{4f} [8, 33]. The major surface defect in CeO_2 assumes oxygen vacancies prevailingly. The location of peaks is the same in the PL spectra of SC. Nevertheless, the intension of the emission band is attenuated, indicating that Sm doping blocks the recombination rate of the holes and electron pairs. It is notable that the characteristic peaks of ASC and AC red-shift to about 420.82 nm and a weaker peak at 486.88 nm , indicating their better visible light response ability. Also, the lower PL intensity of the AC and ASC suggests the lower radiative recombination of the photoexcited carriers (e^- and h^+), which can significantly promote the photocatalytic performance.

Time-resolved photoluminescence (TRPL) lifetime results indicate the ability of the carrier transport layer to extract the carriers. The shorter the TRPL lifetime presents the more potent carrier transfer ability [34]. In consistence with the results of PL spectra, ASC exhibits the fastest

TRPL decay with the lifetime of 0.2728 ns (Figure 4d), which is less than pure CeO₂ (0.3233 ns) and other samples (Figure S7). The shorter TRPL lifetime of ASC suggests a decrease of the exciton population, which further means that the charge separation process is improved and the recombination of the photoinduced electrons and holes is restricted. Therefore, the TRPL result supports the fact that ASC can generate more charge trapping sites which can endow an enhanced photocatalytic activity.

3.3 Photocatalytic evaluation

Here is Figure 5.

Firstly, photooxidation activity of these photocatalysts was tested by removal of gaseous CH₃CHO, which can be described by the reaction of Eq. (4):



As is clearly shown in Figure 5a, the amount of liberated CO₂ reaches a maximum value of about 722.45 ppm for ASC, which is 7.08-times higher than those of the pure CeO₂ (101.96 ppm). Furthermore, the CO₂ liberation amount of ASC is also much higher than that of SC (221.96 ppm) and AC (589.16 ppm). The EPR intensity of ·O₂⁻ in ASC is more robust than pure CeO₂ further reveals the main active specie of the studied photocatalytic material is ·O₂⁻, which is essential for the photocatalytic reactions as highly efficient intermediates in the photocatalytic reactions (Figure 5b). Hence, the improved photocatalytic performance can attribute to a higher concentration of O_v and active oxygen species, and this discovery is consistent with the analysis of Raman and XPS. Notably, the prepared ASC in this study shows superior activity for CH₃CHO oxidation than that of the commercially available metal oxide photocatalysts such as P25 (21 ppm), sulfur-doped TiO₂ (150 ppm) and tungsten oxide (200 ppm) [33, 35].

The photoreduction activity of the as-prepared materials is shown in [Figure 5c](#). The amount of hydrogen (H_2) generated from water-splitting increases linearly with time for all the samples. After visible light radiation for 2.5 h, the H_2 liberation rate of ASC reaches $342.12 \mu\text{mol}\cdot\text{g}^{-1}\cdot\text{h}^{-1}$, which is 6.83-times exceeding those value of CeO_2 ($50.07 \mu\text{mol}\cdot\text{g}^{-1}\cdot\text{h}^{-1}$) ([Figure 5d](#)). Besides, H_2 generation rates of SC and AC are 126.68 and $165.95 \mu\text{mol}\cdot\text{g}^{-1}\cdot\text{h}^{-1}$, respectively, also these values are much lower than those of ASC. Importantly, ASC possesses much better recyclability than AC, indicating that the doping of Sm ions makes the structure of CeO_2 anchored Ag QDs more stable ([Figure S8](#)). In general, it is also necessary to characterize the products with Pt particles loading using transient photocurrent, PL and TRPL results to confirm the radiative recombination rate of the photogenerated electrons and holes ([Figure S9](#)). However, H_2 liberation rate from water splitting without Pt loading of ASC only reaches $42.88 \mu\text{mol}\cdot\text{g}^{-1}\cdot\text{h}^{-1}$, which is lower than those value of pure CeO_2 with 3% Pt loading ($50.07 \mu\text{mol}\cdot\text{g}^{-1}\cdot\text{h}^{-1}$). Similar to the gas phase photo-oxidation, the as-prepared ASC photocatalyst also shows enhanced photocatalytic performance in the liquid medium, e.g., oxidation of bisphenol A (BPA) and reduction of 4-nitrophenol (4-NP) ([Figure S10-S14](#)).

The reason behind the stability of silver loaded in SC is interesting though in general the loading of silver on the surface of a semiconductor is unstable. Hence the first principal method was explored to investigate the mechanism and the results are summarized in [Table S5](#). The total energy of SC is found to be higher than pure CeO_2 , which suggests that CeO_2 can be activated by the doping of Sm. Negative adsorption energy values of ASC and AC indicate that Ag loading on both the materials is favorable. More negative E_{ads} of the ASC compared to the AC can be attributed to the generation of oxygen vacancies [36-38]. The shorter distance between the Ag

cluster and the slab in ASC means that oxygen vacancies can capture the silver clusters and further stabilize the system.

4. Theoretical calculations and possible photocatalytic mechanism

Here is Figure 6.

In order to determine the transfer direction of the charges between Ag QDs and CeO₂ microspheres, SPV technique was applied (Figure 6a). The SPV spectra of all the synthetic samples exhibit the largest broadband at 325 nm, that may cause by a band-to-band transition of photogenerated excitons in intrinsic CeO₂ [39]. Among them, the positive response of CeO₂ and SC indicates that holes transfer to the illumination side of photocatalysts, which can be attributed to the bandgap transition [40]. In contrast, the negative response of AC and ASC means that electrons are transferred to the surface of the irradiated side mainly. In addition, the SPV intensity of ASC was significantly enhanced compared to other samples, which could be attributed to more electrons that will transfer to the CeO₂ surface to form photovoltage. However, the SPV signal for ASC shows distinctive peaks located at 400-500 nm, which considered to be the reduction co-catalyst role of silver in the visible region [41, 42]. After forming a heterogeneous interface between the CeO₂ and the metallic Ag QDs, the Fermi energy levels of two components can reach equilibrium. Then, the electrons in the conduction band of Sm-CeO₂ will inject into the Ag surface under visible light irradiation, resulting in efficient separation of electrons and holes [43, 44].

TPV technology is also an effective mean to reveal the separation and recombination processes of those photo-generated charges in nanomaterials (Figure 6b). First, the TPV signal of the ASC is negative, which indicates that the photoexcited electrons move faster than the holes [42, 45]. It is mainly attributed to Ag's lower potential barrier and superior electronic reception

ability. The rapid diffusion of electrons from CeO₂ to Ag reduces the recombination rate of those photoexcited electrons and holes. The higher TPV intensity caused by significant absorption of ASC than any other samples suggests rapid diffusion of charge carriers, which is also consistent with the TRPL results. Secondly, two response peaks can be observed in the TPV response of ASC. The peak time of P1 is shorter than 10⁻⁶ s, which was attributed to the photogenic charge caused by laser irradiation on ASC and the charge separation caused by the electric field in the surface charge area [42, 46]. In addition, the longer time of P2 peak than 10⁻⁴ s may occur due to the diffusion voltage, and diffusion PV is mainly determined according the concentration of photoexcited charges and the correlative diffusion rate of electrons and holes [45, 46].

Here is Figure 7.

The heterogeneous interface between the SC and the metallic silver was further calculated via by the density functional theory (DFT). According to the charge density difference in [Figure 7a](#), the electrons transfer from SC (yellow region) to the metallic silver side (cyan area), which is consistent with experimental SPV and TPV test. The total and partial density of states (DOS) of ASC are both displayed in [Figure. S15](#), the valence-band maximum (VBM) of heterogeneous ASC is composed of Ag 5s, Ce 4f and Sm 4f orbitals, and conduction-band minimum (CBM) are mainly composed of O 2p orbitals. The charge transfer in the systems of Pt particle and Ag particle co-loaded Sm-doped CeO₂ (PASC) was further considered ([Figure 7b-c](#)). Since the electron affinity of Ag was much higher than CeO₂, the Pt particles tend to be loaded just close to Ag particle [Figure. S16](#). According to the previous literature, Pt particles could serve as an efficient co-catalyst for hydrogen evolution reaction. The boosted charge transfer from ASC to Pt could result in a significantly improved HER performance [47]. Therefore, the addition of co-catalyst Pt is

favorable for accumulation of electrons, which is significantly beneficial to the process of photocatalytic H₂ evolution.

During photocatalysis, a key role is played by the reactive oxygen species and hence it is vital to explore the interaction between the oxygen and photocatalyst and the results are summarized in [Table S6](#). Negative adsorption energy values for all the materials indicate that the interactions between oxygen and the CeO₂ based photocatalysts are positive with the order of the interaction energy being: ASC-O > CeO₂-O > SC-O. It indicates that oxygen adsorbed on the ASC is the most reactive photocatalyst [36-38]. The adsorption energy directly reflects the photocatalysts oxygen adsorption capacity. The results show that adsorption energies of ASC and SC are larger than that of CeO₂, which means that the oxygen vacancies can stabilize oxygen (many theoretical results have confirmed this hypothesis). As a result, the distance between the oxygen and the surface of the photocatalysts is dramatically shortened. It is noteworthy that the distance between oxygen and ASC is only 0.065 Å. It is fascinating that the oxygen vacancy is almost occupied by one oxygen atom. The most critical parameter is the bond distance of oxygen, because it shows the nature of the adsorbed oxygen. The original O-O bond length is 1.225 Å, and when the oxygen is adsorbed on the photocatalyst, it will change the bond length. The bond length of the oxygen on the CeO₂ surface is almost the same as the original value, indicating that the interaction between the oxygen and CeO₂ is simply physical adsorption. The bond length of the oxygen on the surface of SC is longer than 1.3 Å, which means that the interaction between the oxygen and SC is chemical adsorption by nature with the formation of superoxide ($\cdot\text{O}_2^-$). A shorter distance between the oxygen and the photocatalyst surface due to the oxygen vacancy results in the loss of one electron from the nearby Ce³⁺ which is then transported to the adsorbed oxygen, thus forming $\cdot\text{O}_2^-$. When the Ag was loaded on the surface of the SC, the bond length of the oxygen on the surface became

1.434 Å, indicating the formation of peroxide species ($\cdot\text{O}_2^{2-}$). The introduction of Ag not only shortens the distance between the oxygen and ASC, but also lengthens the O-O bond. We speculate that in the peroxide anion, one electron is supplied from the Ce^{3+} nearby the oxygen vacancy, and the other electron is supplied from Ag. The generated reactive oxygen species will accelerate the photocatalytic reactions.

Accordingly, a reasonable mechanism for the enhanced photocatalytic property of ASC is proposed (Figure 7d). After the doping of Sm ions, an increased concentration of oxygen vacancies (O_v) is generated resulting in the construction of a transition energy state and it is closer to the conduction band (CB), attributing to the reduction of the bandgap. Under visible light irradiation, the doping-related transition level can capture the photoexcited electrons in Sm-doped CeO_2 and limit the recombination of the photoinduced electron and hole pairs efficiently. Then, these captured electrons further transferred to the Ag QDs via the heterogeneous interface between the SC and the metallic silver, and Ag induces improvement of the visible light absorption capacity synchronously. During the process of photocatalysis, transferred electrons on the silver will act as active sites for water reduction splitting as well as oxygen activation. Notably, more separated holes will be photo-induced, which are beneficial for the generation of reactive oxygen species. And they are efficient intermediates with vivid photocatalytic oxidation ability for involved photocatalytic redox reactions. To sum up, in comparison to those traditional semiconductor photocatalysts, the visible-light-driven CeO_2 achieved by Sm doping and Ag QDs anchoring in this paper is bound to enhance the photocatalytic performance.

5. Conclusions

In summary, silver quantum dots modified Sm-doped CeO_2 photocatalyst was successfully

synthesized using a one-step hydrothermal mean. This strategy is efficient, reproducible and can be branch out into the fabrication of other ceria-based inorganic nanomaterials. The structure and morphology information of ASC were characterized by XRD, HR-TEM and FE-SEM. The features of optics, defects and chemical states were investigated by Raman, UV-vis, XPS, PL and TRPL. For instance, ASC affords 7.08-times and 6.83-times higher CH_3CHO conversion to CO_2 and water reduction to generate hydrogen than those of untreated CeO_2 , respectively. Furthermore, as-prepared ASC exhibits similarly improved photocatalytic activities for photooxidation of BPA and photoreduction of 4-NP. Own to the presence of a higher Sm ions doping-related concentration of O_v in ASC, it can lower the bandgap energy (E_g) and limit the recombination of the photoexcited electron and holes. In addition, the improved visible light response of Ag QDs shows an equally significant role in the photocatalytic process. Therefore, the elaborated ASC heterogeneous photocatalyst with waxberry-like morphology in this study can pave the way for the fabrication of other cost-effective photocatalysts in many prospective applications.

Acknowledgements

This work was financially supported by the Natural Science Foundation of China (No. 21805191 and No. 21307104), the Guangdong Basic and Applied Basic Research Foundation (2020A151501982), the Major Projects of Nature Science Research in Universities and Colleges in Jiangsu Province, China (No. 16KJA150008), Shenzhen Peacock Plan (No. 20180921254c) and the JST ACT-C program of Japan. The authors thank Tsinghua National Laboratory for Information Science and Technology for providing grid resources that contributed to the calculation results. Prof. Tengfeng Xie and Dr. Kai Zhang from Jilin University are also acknowledged for their help in SPV and TPV characterization.

Associated Contents

Supporting Information is available from the Publications online version or from the authors. Experimental characterization, experiments of Bisphenol A photooxidation, 4-nitrophenol photoreduction and active species trapping. Figure. S1-S16 and Table. S1-S6.

Declaration of Interests

The authors declare no conflicts of financial interest.

References

- (1) Montini, T.; Melchionna, M.; Monai, M.; Fornasiero, P., Fundamentals and Catalytic Applications of CeO₂-Based Materials, *Chem Rev*, 116 (2016) 5987-6041.
- (2) Mahadi, A. H.; Ye, L.; Fairclough, S. M.; Qu, J.; Wu, S.; Chen, W.; ect., Beyond surface redox and oxygen mobility at Pd-polar ceria (100) interface: Underlying principle for strong metal-support interactions in green catalysis, *Appl. Catal. B: Environ.*, 270 (2020) 118843.
- (3) Pan, L.; Ai, M.; Huang, C.; Yin, L.; Liu, X.; Zhang, R.; Wang, S.; Jiang, Z.; Zhang, X.; Zou, J. J.; Mi, W., Manipulating spin polarization of titanium dioxide for efficient photocatalysis, *Nat Commun*, 11 (2020) 418.
- (4) Naghavi, S. S.; Emery, A. A.; Hansen, H. A.; Zhou, F.; Ozolins, V.; Wolverton, C., Giant onsite electronic entropy enhances the performance of ceria for water splitting, *Nat Commun.*, 8 (2017), 285-291.
- (5) Wang, Z.; Yu, R., Hollow Micro/Nanostructured Ceria-Based Materials: Synthetic Strategies and Versatile Applications, *Adv Mater.*, 31 (2019) 1800592.
- (6) Shang, H.; Huang, S.; Li, H.; Li, M.; Zhao, S.; Wang, J.; Ai, Z.; Zhang, L., Dual-site activation enhanced photocatalytic removal of no with Au/CeO₂. *Chem Eng J*. 386 (2020) 124047.
- (7) Hammond, O. S.; Edler, K. J.; Bowron, D. T.; Torrente-Murciano, L., Deep eutectic-solvothermal synthesis of nanostructured ceria, *Nat Commun.*, 8 (2017) 14150.

- (8) Yang, H.; Xu, B.; Yuan, S.; Zhang, Q.; Zhang, M.; Ohno, T., Synthesis of Y-doped CeO₂/PCN nanocomposited photocatalyst with promoted photoredox performance, *Appl. Catal. B: Environ.*, 243 (2019) 513-521.
- (9) Xu, B.; Zhang, Q.; Yuan, S.; Zhang, M.; Ohno, T., Morphology control and characterization of broom-like porous CeO₂, *Chemical Engineering Journal.*, 260 (2015) 126-132.
- (10) Yuan, S.; Zhang, Q.; Xu, B.; Jin, Z.; Zhang, Y.; Yang, Y.; Zhang, M.; Ohno, T., Porous cerium dioxide hollow spheres and their photocatalytic performance, *RSC Adv.*, 4 (2014) 62255-62261.
- (11) Zhang, S.; Huang, Z. Q.; Ma, Y.; Gao, W.; Li, J.; Cao, F.; Li, L.; Chang, C. R.; Qu, Y., Solid frustrated-Lewis-pair catalysts constructed by regulations on surface defects of porous nanorods of CeO₂, *Nat Commun.*, 8 (2017) 15266-15277.
- (12) S, S. M.; Adabifiroozjaei, E.; Yao, Y.; Koshy, P.; Lim, S.; Webster, R.; Liu, X.; Khayyam Nekouei, R.; Cazorla, C.; Liu, Z.; Wang, Y.; Lambropoulos, N.; Sorrell, C. C., Proton-assisted creation of controllable volumetric oxygen vacancies in ultrathin CeO_{2-x} for pseudocapacitive energy storage applications, *Nat Commun.*, 10 (2019) 2594-2600.
- (13) Yang, C.; Li, R.; Zhang, K. A. I.; Lin, W.; Landfester, K.; Wang, X., Wang, Heterogeneous photoredox flow chemistry for the scalable organosynthesis of fine chemicals, *Nat Commun.*, 11 (2020) 1239.
- (14) Pan, F.; Xiang, X.; Du, Z.; Sarnello, E.; Li, T.; Li, Y., Integrating photocatalysis and thermocatalysis to enable efficient CO₂ reforming of methane on Pt supported CeO₂ with Zn doping and atomic layer deposited MgO overcoating. *Appl. Catal. B: Environ.*, 260 (2020) 118189.
- (15) Song, S.; Li, K.; Pan, J.; Wang, F.; Li, J.; Feng, J.; Yao, S.; Ge, X.; Wang, X.; Zhang, H., Achieving the Trade-Off between Selectivity and Activity in Semihydrogenation of Alkynes by Fabrication of (Asymmetrical Pd@Ag Core)@(CeO₂ Shell) Nanocatalysts via Autoredox Reaction, *Adv Mater.*, 29 (2017) 1605332.
- (16) Carltonbird, M.; Eaimsumang, S.; Pongstabodee, S.; Boonyuen, S.; Smith, S. M.; Luengnaruemitchai, A., Effect of the exposed ceria morphology on the catalytic activity of gold/ceria catalysts for the preferential oxidation of carbon monoxide, *Chem Eng J.*, 344 (2018) 545-555.

- (17) Ye, L.; Duan, X.; Wu, S.; Wu, T. S.; Zhao, Y.; Robertson, A. W.; Chou, H. L.; Zheng, J.; Ayvali, T.; Day, S.; Tang, C.; Soo, Y. L.; Yuan, Y.; Tsang, S. C. E., Self-regeneration of Au/CeO₂ based catalysts with enhanced activity and ultra-stability for acetylene hydrochlorination, *Nat Commun.*, 10 (2019) 914.
- (18) Peng, H.; Dong, T.; Zhang, L.; Wang, C.; Liu, W.; Bao, J.; Wang, X.; Zhang, N.; Wang, Z.; Wu, P.; Zhang, P.; Dai, S., Active and stable Pt-Ceria nanowires@silica shell catalyst: Design, formation mechanism and total oxidation of CO and toluene. *Appl. Catal. B: Environ.*, 256 (2019) 117807.
- (19) Kwak, N. W.; Jeong, S. J.; Seo, H. G.; Lee, S.; Kim, Y.; Kim, J. K.; Byeon, P.; Chung, S. Y.; Jung, W., In situ synthesis of supported metal nanocatalysts through heterogeneous doping, *Nat Commun.*, 9 (2018) 4829.
- (20) Jiang, R.; Li, B.; Fang, C.; Wang, J., Metal/Semiconductor hybrid nanostructures for plasmon-enhanced applications, *Adv Mater.*, 26 (2014) 5274-309.
- (21) Yu, L.; Peng, R. S.; Chen, L. M.; Fu, M. L.; Wu, J. L.; Ye, D. Q., Ag supported on CeO₂ with different morphologies for the catalytic oxidation of HCHO. *Chem Eng J*, 334 (2018) 2480-2487.
- (22) Grabchenko, M. V.; Mamontov, G. V.; Zaikovskii, V. I.; La Parola, V.; Liotta, L. F.; Vodyankina, O. V., The role of metal-support interaction in Ag/CeO₂ catalysts for CO and soot oxidation. *Appl. Catal. B: Environ.*, 260 (2020) 118148.
- (23) Pereira-Hernandez, X. I.; DeLaRiva, A.; Muravev, V.; Kunwar, D.; Xiong, H.; Sudduth, B.; Engelhard, M.; Kovarik, L.; Hensen, E. J. M.; Wang, Y.; Datye, A. K., Tuning Pt-CeO₂ interactions by high-temperature vapor-phase synthesis for improved reducibility of lattice oxygen, *Nat Commun.*, 10 (2019) 1358.
- (24) Wang, A.; Zheng, Z.; Wang, H.; Chen, Y.; Luo, C.; Liang, D.; Hu, B.; Qiu, R.; Yan, K., 3D hierarchical H₂-reduced Mn-doped CeO₂ microflowers assembled from nanotubes as a high-performance Fenton-like photocatalyst for tetracycline antibiotics degradation, *Appl. Catal. B: Environ.*, 277 (2020) 119171.
- (25) Gopal, C. B.; Gabaly, F. E.; McDaniel, A. H.; Chueh, W. C., Origin and Tunability of Unusually Large Surface Capacitance in Doped Cerium Oxide Studied by Ambient-Pressure X-Ray Photoelectron Spectroscopy, *Adv Mater.*, 28 (2016) 4692-4697.

- (26) Yang, S. M.; Lee, S.; Jian, J.; Zhang, W.; Lu, P.; Jia, Q.; Wang, H.; Noh, T. W.; Kalinin, S. V.; MacManus-Driscoll, J. L., Strongly enhanced oxygen ion transport through samarium-doped CeO₂ nanopillars in nanocomposite films, *Nat Commun.*, 6(2015) 8588.
- (27) Zhu, H.; Yang, C.; Li, Q.; Ren, Y.; Neufeind, J. C.; Gu, L.; Liu, H.; Fan, L.; Chen, J.; Deng, J.; Wang, N.; Hong, J.; Xing, X., Charge transfer drives anomalous phase transition in ceria, *Nat Commun.*, 9 (2018) 5063.
- (28) Xu, B.; Yang, H.; Zhang, Q.; Yuan, S.; Xie, A.; Zhang, M.; Ohno, T., Design and Synthesis of Sm, Y, La and Nd-doped CeO₂ with a broom-like hierarchical structure: a photocatalyst with enhanced oxidation performance, *ChemCatChem*, 12 (2020) 2638-2646.
- (29) Xu, B.; Zhang, Q.; Yuan, S.; Zhang, M.; Ohno, T., Synthesis and photocatalytic performance of yttrium-doped CeO₂ with a porous broom-like hierarchical structure, *Appl. Catal. B: Environ.*, 183 (2016) 361-370.
- (30) O'Neill, D. B.; Prezgot, D.; Ianoul, A.; Otto, C.; Mul, G.; Huijser, A., Silver Nanocubes Coated in Ceria: Core/Shell Size Effects on Light-Induced Charge Transfer, *ACS Appl Mater Interfaces*, 12 (2020) 1905-1912.
- (31) Jampaiah, D.; Ippolito, S. J.; Sabri, Y. M.; Reddy, B. M.; Bhargava, S. K., Highly efficient nanosized Mn and Fe codoped ceria-based solid solutions for elemental mercury removal at low flue gas temperatures, *Catalysis Science & Technology*, 5 (2015) 2913-2924.
- (32) Venkataswamy, P.; Jampaiah, D.; Kandjani, A. E.; Sabri, Y. M.; Reddy, B. M.; Vithal, M., Transition (Mn, Fe) and rare earth (La, Pr) metal doped ceria solid solutions for high performance photocatalysis: Effect of metal doping on catalytic activity, *Research on Chemical Intermediates*, 44 (2017) 2523-2543.
- (33) Zhang, Q.; Yuan, S.; Xu, B.; Xu, Y.; Cao, K.; Jin, Z.; Qiu, C.; Zhang, M.; Su, C.; Ohno, T., A facile approach to build Bi₂O₂CO₃/PCN nanohybrid photocatalysts for gaseous acetaldehyde efficient removal, *Catalysis Today*, 315 (2018) 184-193.
- (34) Mansingh, S.; Padhi, D. K.; Parida, K. M., Enhanced visible light harnessing and oxygen vacancy promoted N, S co-doped CeO₂ nanoparticle: a challenging photocatalyst for Cr(VI) reduction, *Catalysis Science & Technology*, 7 (2017) 2772-2781.

- (35) Jin, Z.; Murakami, N.; Tsubota, T.; Ohno, T., Complete oxidation of acetaldehyde over a composite photocatalyst of graphitic carbon nitride and tungsten(VI) oxide under visible-light irradiation, *Appl. Catal. B: Environ.*, 150-151 (2014) 479-485.
- (36) Zhao, L.; Wu, Y.; Han, J.; Lu, Q.; Yang, Y.; Zhang, L., Mechanism of Mercury Adsorption and Oxidation by Oxygen over the CeO₂ (111) Surface: A DFT Study, *Materials (Basel)*, 11 (2018) 485.
- (37) Sawabe, K.; Yoshikawa, Y.; Satsuma, A., Density-Functional Theoretical Study on the Role of Lewis and Brønsted Acid Sites on CeO₂ (110) Surfaces for Nitrile Hydration, *Topics in Catalysis*, 57 (2014) 1094-1102.
- (38) Zhang, Y.-C.; Li, Z.; Zhang, L.; Pan, L.; Zhang, X.; Wang, L.; Fazal e, A.; Zou, J.-J., Role of oxygen vacancies in photocatalytic water oxidation on ceria oxide: Experiment and DFT studies, *Appl. Catal. B: Environ.*, 224 (2018) 101-108.
- (39) Zhang, N.; Li, G.; Xie, T.; Li, L., Amorphous tantalum oxyhydroxide homojunction: In situ construction for enhanced hydrogen production, *J Colloid Interface Sci.*, 525 (2018) 196-205.
- (40) Fang, S.; Li, S.; Ge, L.; Han, C.; Qiu, P.; Gao, Y., Synthesis of novel CoO_x decorated CeO₂ hollow structures with an enhanced photocatalytic water oxidation performance under visible light irradiation, *Dalton Trans.*, 46 (2017) 10578-10585.
- (41) Wang, X.; Wu, T.; Wang, H.; Su, X., Interesting electron storage phenomenon in the spherical Ag/TiO₂ nanocomposites and its application for the decomposition of acetaldehyde in the dark, *Materials Research Bulletin*, 73 (2016) 423-428.
- (42) Mu, Z.; Yan, W.; Zhao, R.; Lin, Y., Study on the photogenerated charge transfer and photoelectrocatalytic performance of Ag/ZnO nanorod arrays under the irradiation of simulated sun light, *Materials Research Express*, 2 (2019) 065008.
- (43) Zhou, Q.; Ma, S.; Zhan, S., Superior photocatalytic disinfection effect of Ag-3D ordered mesoporous CeO₂ under visible light, *Appl. Catal. B: Environ.*, 224 (2018) 27-37.
- (44) Ouyang, X.; Tang, L.; Feng, C.; Peng, B.; Liu, Y.; Ren, X.; Zhu, X.; Tan, J.; Hu, X., Au/CeO₂/g-C₃N₄ heterostructures: Designing a self-powered aptasensor for ultrasensitive detection of Microcystin-LR by density functional theory, *Biosens Bioelectron.*, 164 (2020) 112328.

(45) Zhang, L. J.; Li, S.; Liu, B. K.; Wang, D. J.; Xie, T. F., Highly Efficient CdS/WO₃ Photocatalysts: Z-Scheme Photocatalytic Mechanism for Their Enhanced Photocatalytic H₂ Evolution under Visible Light, ACS Catalysis, 4 (2014) 3724-3729.

(46) Moradi, M.; Moussavi, G.; Yaghmaeian, K.; Yazdanbakhsh, A.; Srivastava, V.; Sillanpää, M., Synthesis of novel Ag-doped S-MgO nanosphere as an efficient UVA/LED-activated photocatalyst for non-radical oxidation of diclofenac: Catalyst preparation and characterization and photocatalytic mechanistic evaluation, Appl. Catal. B: Environ., 260 (2020) 118128.

(47) Q. Wang, K. Domen, Particulate Photocatalysts for Light-Driven Water Splitting: Mechanisms, Challenges, and Design Strategies, Chem Rev, 120 (2020) 919-985.

Figure captions

Figure 1. TEM images of (a) CeO₂, (b) SC, (c) AC, (d) ASC, (e) HR-TEM images of ASC, and (f) lattice fringe in ASC.

Figure 2. (a) XRD patterns, (b) detailed view of the highest (111) peak patterns, (c) Raman spectra and (d) enlarged view of Raman spectra.

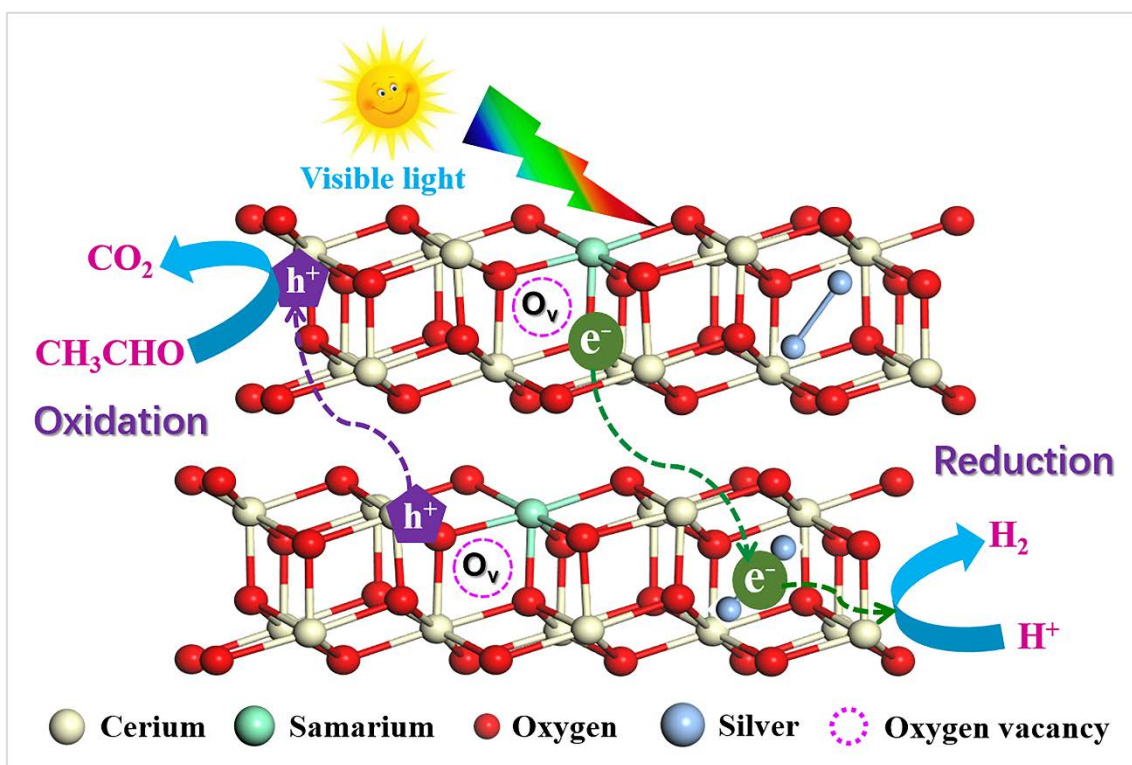
Figure 3. Separated peak curves of (a) Ce 3d, (d) O 1s, high-resolution XPS spectra of (b) Ce 3d, (c) Ag 3d, (e) O 1s and (d) Sm 3d of as-prepared samples.

Figure 4. (a) UV diffuse reflectance spectra, (b) transient photocurrent response, (c) PL spectra of samples and (d) TRPL spectra of ASC and CeO₂.

Figure 5. (a) Time course of CO₂ liberation from CH₃CHO decomposition and (b) EPR spectra of ·O₂⁻ in ASC and CeO₂, (c) Time course of H₂ liberation from water splitting and (d) evolution rate curve of samples.

Figure 6. (a) SPV spectra and (b) TPV spectra of as-prepared samples. The wavelength and intensity of excitation pulse are 355 nm and 50 μJ, respectively. Inset: schematic setup of TPV measurement.

Figure 7. Calculated cross view charge density differences of (a) ASC, (b) Ag and Pt particles co-loaded on the surface of the ASC, (c) Pt particles loaded on the surface of the Ag particle, (Color: Ce, yellow; O, red; Sm, rose; Ag, gray; Pt, argent) and (d) proposed mechanism for enhanced photocatalytic performance of CH₃CHO decomposition and water splitting.



Graphical abstract

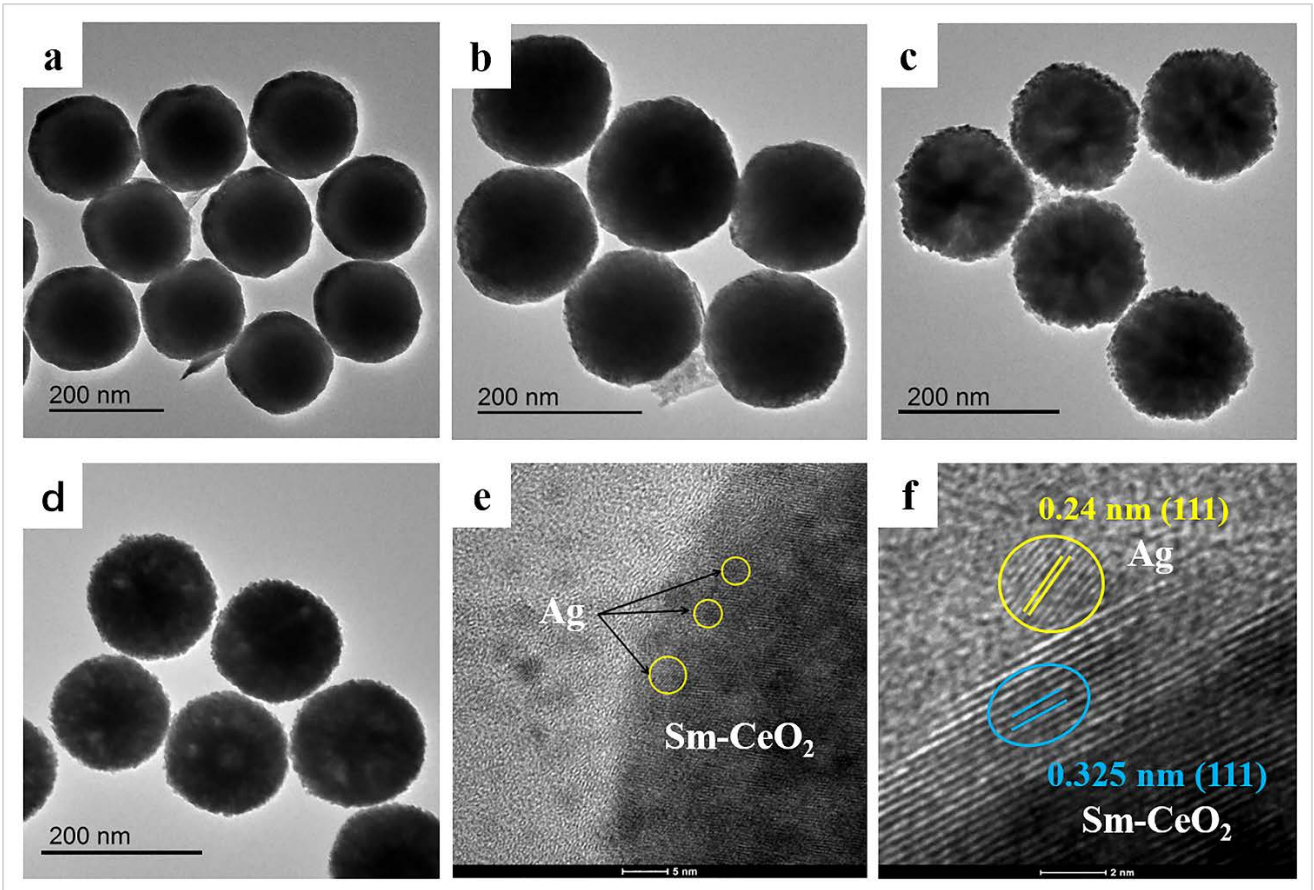


Fig.1

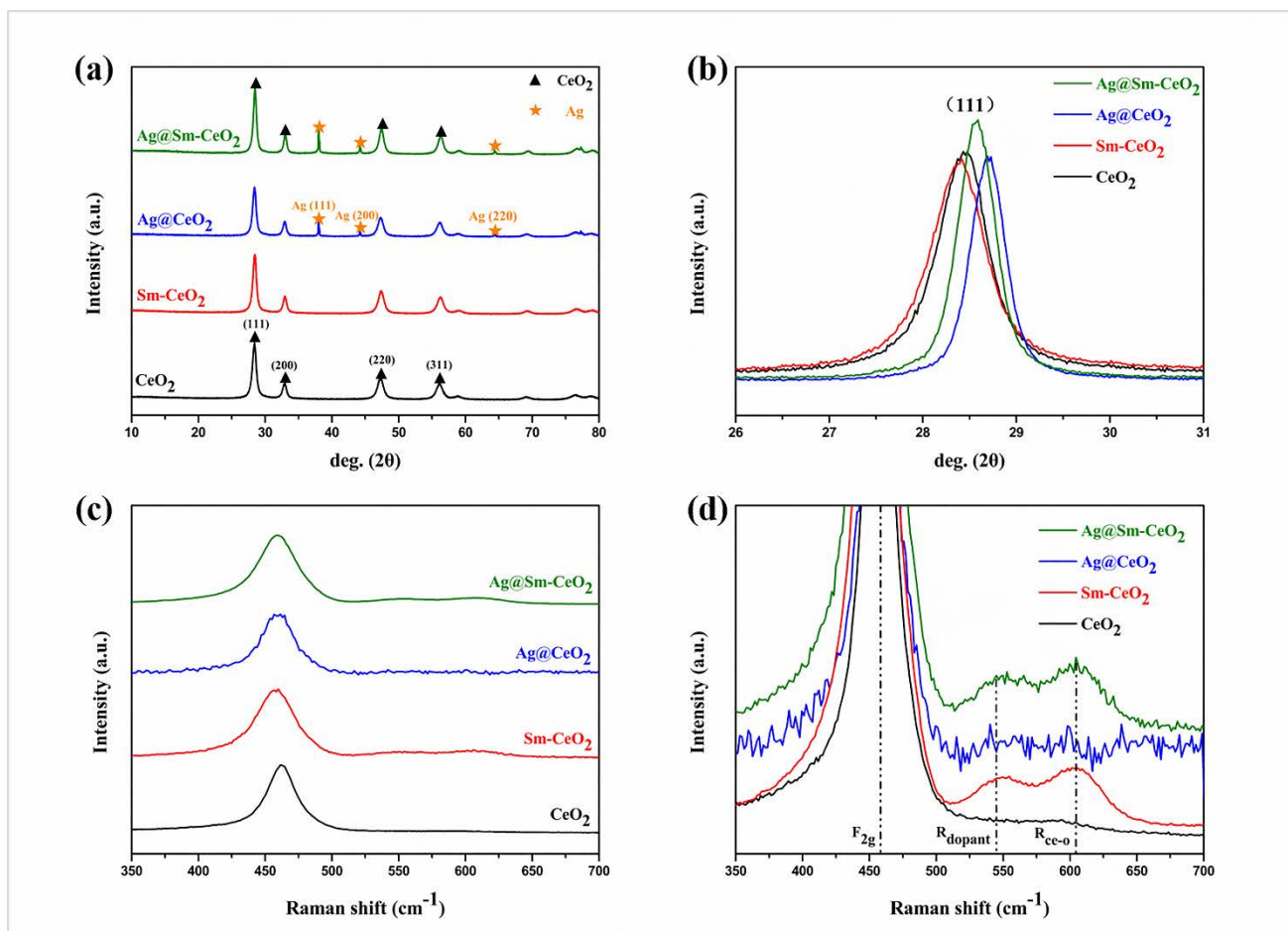


Fig.2

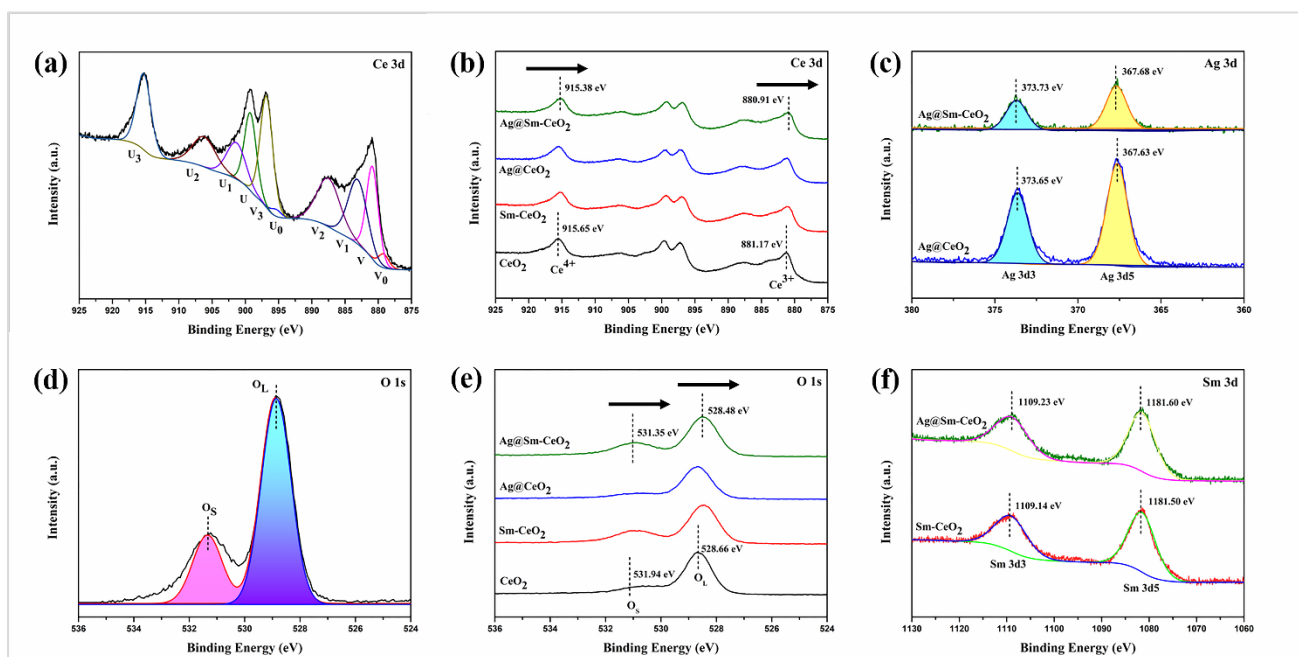


Fig.3

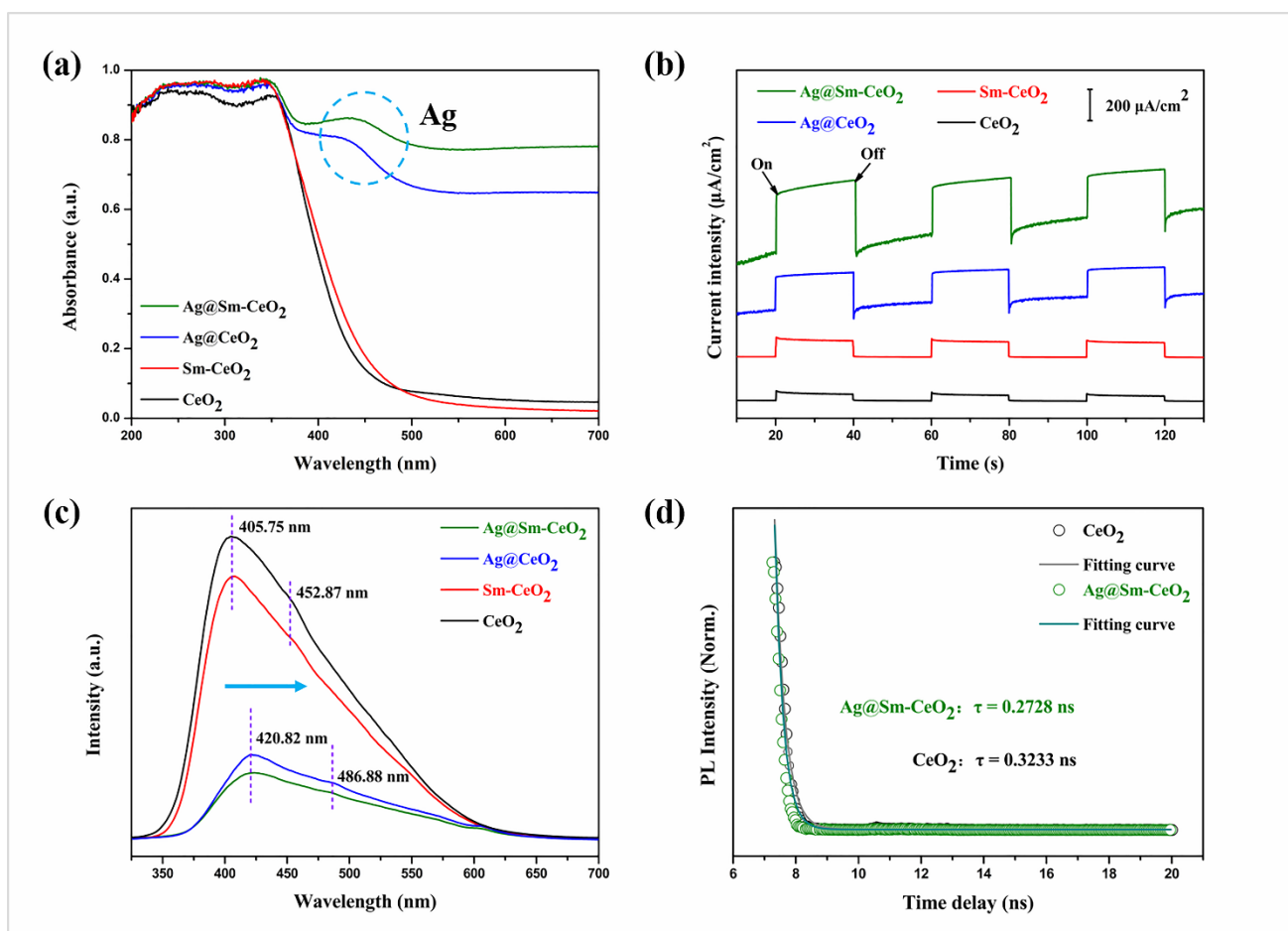


Fig.4

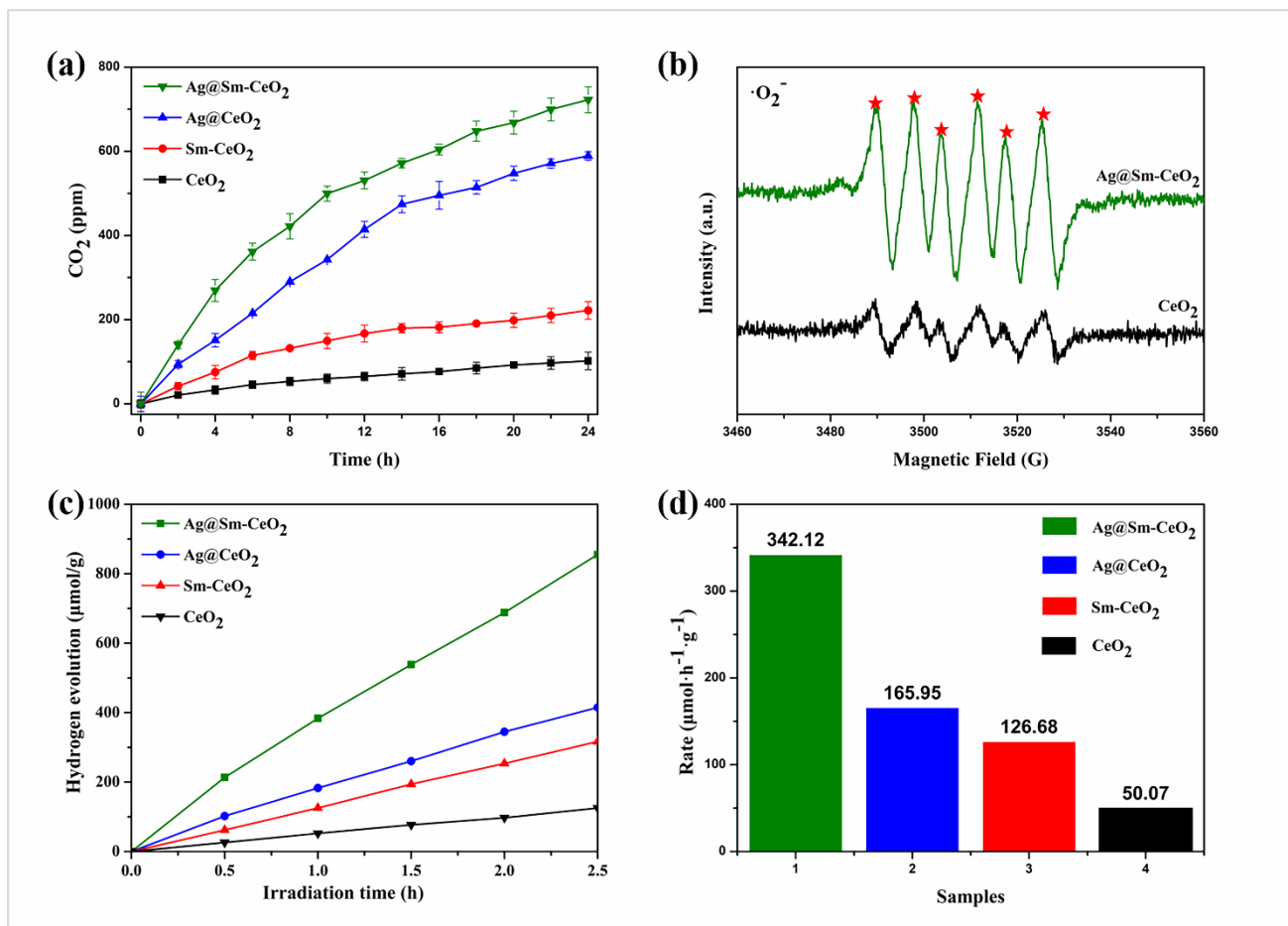


Fig.5

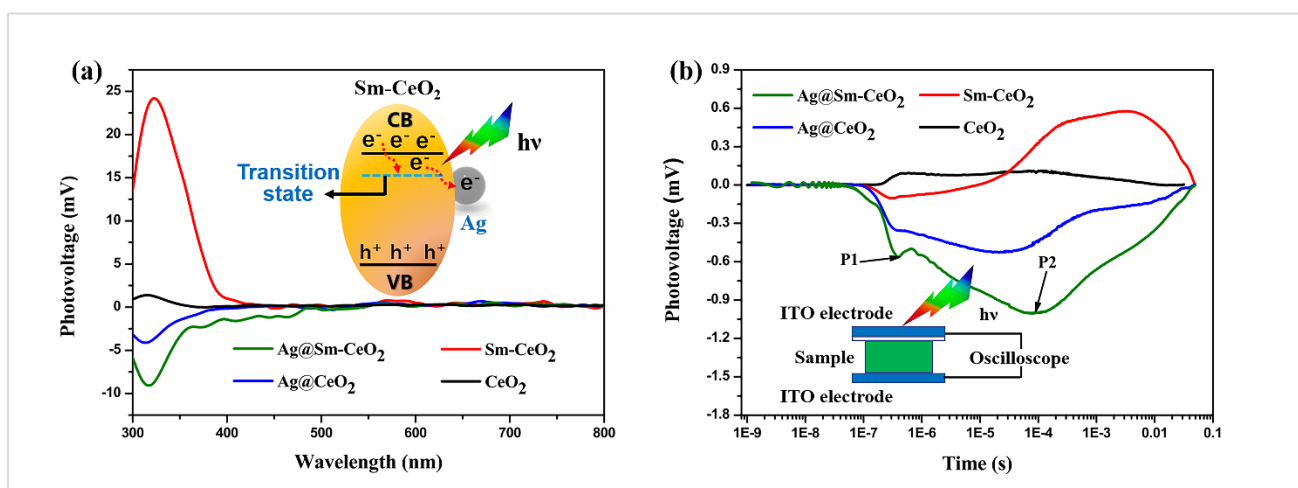


Fig.6

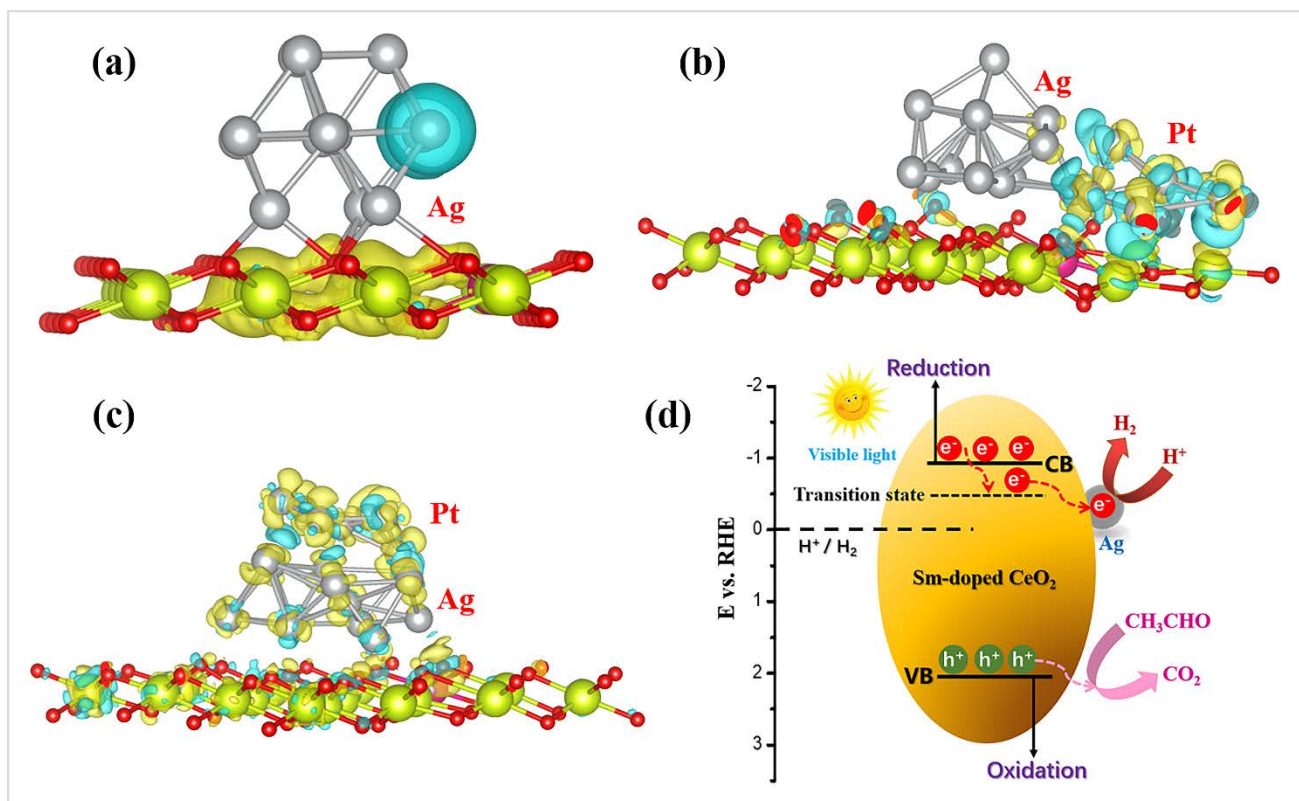


Fig.7